

# Hot isostatic pressing influence on the mechanical properties of selectively laser-melted 316L steel

J. KLUCZYŃSKI<sup>1\*</sup>, L. ŚNIEŻEK<sup>1</sup>, K. GRZELAK<sup>1</sup>, A. OZIĘBŁO<sup>2</sup>, K. PERKOWSKI<sup>2</sup>,  
J. TORZEWSKI<sup>1</sup>, I. SZACHOGŁUCHOWICZ<sup>1</sup>, K. GOCMAN<sup>3</sup>, M. WACHOWSKI<sup>1</sup>,  
and B. KANIA<sup>4</sup>

<sup>1</sup>Military University of Technology, Faculty of Mechanical Engineering, Institute of Robots & Machine Design,  
ul. Gen. S. Kaliskiego 2, 00-908 Warsaw 49, Poland

<sup>2</sup>Institute of Ceramics and Building Materials, Department of Ceramics and Composites, ul. Postępu 9, 02-676 Warsaw, Poland

<sup>3</sup>Military University of Technology, Faculty of Mechanical Engineering, Institute of Vehicles & Transportation,  
ul. Gen. S. Kaliskiego 2, 00-908 Warsaw 49, Poland

<sup>4</sup>Institute of Metallurgy and Materials Science, Polish Academy of Sciences, ul. Reymonta 25, 30-059 Krakow, Poland

**Abstract.** Industries that rely on additive manufacturing of metallic parts, especially biomedical companies, require material science-based knowledge of how process parameters and methods affect the properties of manufactured elements, but such phenomena are incompletely understood. In this study, we investigated the influence of selective laser melting (SLM) process parameters and additional heat treatment on mechanical properties. The research included structural analysis of residual stress, microstructure, and scleronomic hardness in low-depth measurements. Tensile tests with specimen deformation analysis using digital image correlation (DIC) were performed as well. Experiment results showed it was possible to observe the porosity growth mechanism and its influence on the material strength. Specimens manufactured with 20% lower energy density had almost half the elongation, which was directly connected with the porosity growth during energy density reduction. Hot isostatic pressing (HIP) treatment allowed for a significant reduction of porosity and helped achieve properties similar to specimens manufactured using different levels of energy density.

**Key words:** 316L austenitic steel, selective laser melting, hot isostatic pressing, microscopic investigation, residual stresses.

## 1. Introduction

Research on additive manufacturing with metal powders [1] has grown significantly, yet many research questions remain unanswered. The intensity of the research is driven by the wide use of additive manufacturing to make geometrically complex parts in fields such as medical devices [2], aviation [3], automotive [4], and metallurgy industry [5] and other mechanical solutions [6].

One area of ongoing investigation concerns the modification of the mechanical properties of additively manufactured parts. Both the layer-by-layer characteristics of the process and the use of process parameters allow for the control of manufactured element properties through a variety of methods, including process parameter modification [7], heat treatment after selective laser melting (SLM) processing [8, 9], 3D model topology [10–13], and surface treatment after SLM processing [14]. A proper surface parameter has a significant influence on the mechanical properties, which was deeply investigated by Macek *et al.* [15] in their work. Parameter modification can be used to increase the process efficiency or to customize the properties of manufactured parts for a specific application, such as increasing the porosity in plain bearings construction.

The most significant property that changes with process parameters, even within small ranges of parameter modification, is porosity. Additively manufactured elements made using powder bed fusion (PBF) technologies are characterized by low porosity, e.g. lower than 1% [16–18]. However, in some cases, increased porosity is a desired effect. The best examples of this are certain medical applications where porosity is appropriate. Most additively manufactured elements are designed in such a way that its mechanical properties can be modified without decreasing the material porosity. To accomplish structural modification, the most significant factor is the use of the proper type of heat treatment to achieve an acceptable microstructure.

Some types of heat treatment assure the modification of material properties, but without porosity reduction. To achieve porosity reduction, hot isostatic pressing (HIP) can be an appropriate method of heat treatment. The HIP process results in a reduction in the number of pores in the material structure after additive manufacturing processing [19, 20]. Despite this, many studies [21–23] report that HIP treatment positively affects material properties by reducing the structural porosity and increasing the material elongation (with the presence of significant load), which eliminate the probability of brittle material cracking. There is also some research on the negative influence of HIP treatment. Geenen *et al.* [24] found undesirable effects on the material properties after HIP including a lack of porosity reduction and also lower corrosion resistance.

\*e-mail: janusz.kluczynski@wat.edu.pl

Manuscript submitted 2020-06-16, revised 2020-08-19, initially accepted for publication 2020-09-14, published in December 2020

Our own previous research results revealed how different technological parameters affect microstructure and mechanical properties based on earlier research [25–27]. This is helpful for understanding when a particular modification method (process parameters, type of heat treatment) would be effective in the design application. In connection with specially designed research programs, this study investigated the influence of five groups of SLM process parameters on austenitic 316L stainless steel structure and mechanical behavior. Groups of parameters were selected from the existing research based on two main properties: porosity and microhardness. To maintain the research continuity, sample indication numbers have been retained from the basic research [8, 26, 28]. It is worth noting that parameter modification in the abovementioned own research was based on the low-ranged ( $\pm 10\%$ ) changes of three values: laser power, hatching distance (the distance between laser lines), and laser exposure velocity. All these parameters form part of the exposure energy density during the SLM process.

One group of selected parameters was taken from research by Di Wang *et al.* [29] which stated that using much higher energy density could ensure better mechanical properties.

## 2. Experimental

**2.1. Material.** The powder (LPW Technology) used for the production of all specimens was gas-atomized 316L steel produced in an argon atmosphere. Based on the scanning electron microscope (SEM) the results are shown in Fig. 1. Powder particles were spherical with a diameter of 15–63  $\mu\text{m}$ .

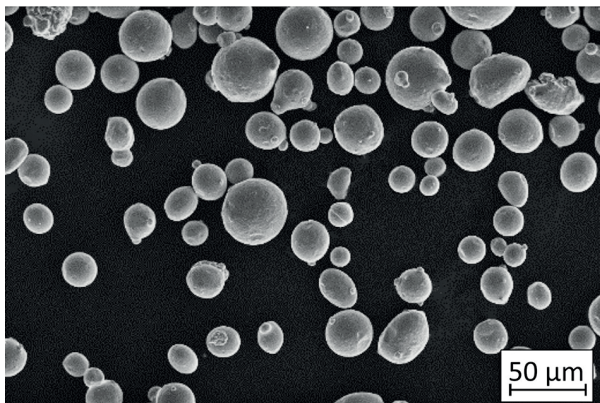


Fig. 1. Scanning electron microscope image of 316L powder particles captured in secondary electron mode

The density of the material was  $7.92 \text{ g/cm}^3$  and its flowability was 14.6 s/50 g. The nominal chemical composition of the material is shown in Table 1.

To verify the chemical composition of powder particles additional analysis has been performed using EDS (electron backscatter diffraction) module in SEM (scanning electron microscope) Jeol JSM-6610 (JEOL Ltd, Tokyo, Japan). The registered data are shown in Table 2.

Table 1  
316L steel nominal chemical composition [30]

Mn	max. 2.00	Si	0.70	P	max. 0.04
S	max. 0.03	N	max. 0.10	Cr	16.00–18.00
Mo	2.00–3.00	Ni	10.00–14.00		

Table 2  
316L steel chemical composition after SEM analysis

Element	Apparent Concentration	Wt [%]	Wt [% Sigma]	Atomic [%]
Si	0.06	1.02	0.09	1.88
Cr	1.35	17.63	0.29	17.61
Fe	4.31	63.06	0.52	58.65
Ni	0.80	12.23	0.42	10.82
Mo	0.14	2.54	0.26	1.37

Lack of elements (Mn, P, S, and N) in the analyzed chemical composition is connected with a very low number of mentioned elements in the registered measurement points.

**2.2. Manufacturing process description.** All specimens were manufactured on the SLM 125HL machine (SLM Solutions AG). All research was conducted on specimens designed according to the ASTM E466–96 standard. To obtain reliable results, all tests including microstructure, residual stress, and hardness analysis were conducted using the same types of specimens. During the process, specimens were oriented in the vertical direction, with the longer specimen edge laid on the building platform surface. For structural and hardness tests, a cutout was taken of each specimen from 7 mm of its tip. The specimen geometry is shown in Fig. 2.

All specimens were designed using SolidWorks 2019 software and manufactured using 316L (1.4404) austenitic steel powder. During the preliminary tests conducted by the authors [26], changes in microhardness and porosity were observed when the selected parameters were modified by 10 percent. During the abovementioned tests, the modified parameters were laser power, laser exposure velocity, and hatching distance.

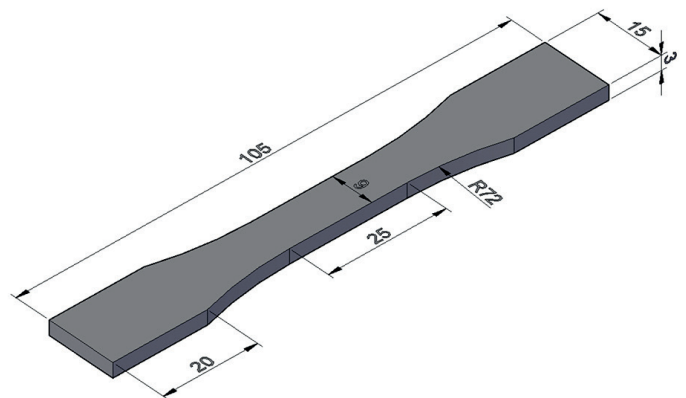


Fig. 2. Specimen dimensions based on the ASTM E466-96 standard

The selection of parameters for modification was made based on their influence on energy density. Following Equation (1), energy density is affected by four different parameters:

$$\rho_E \text{ [J/mm}^3\text{]} = \frac{L_P \text{ [W]}}{e_v \text{ [mm/s]} \cdot h_d \text{ [mm]} \cdot l_t \text{ [mm]}} \quad (1)$$

where:  $L_P$  – laser power [W],  $e_v$  – exposure velocity [mm/s],  $h_d$  – hatching distance [mm],  $l_t$  – layer thickness [mm].

Five different groups of parameters were investigated. The main group consisted of SLM device parameters for 316L steel and was marked as S\_01. The second group consisted of parameters where low porosity was recorded despite an increased hatching distance. This was called the S\_15 group. The third group, marked as S\_17, contained the parameters that recorded the highest porosity during manufacturing with the lowest energy density from all groups.

Of note is the fact that the lowest microhardness values were discovered in samples made using that group of parameters. S\_27 was the parameter group of the specimens with the highest microhardness values. The last group was S\_30, containing parameters with the highest value of energy density based on the literature. All described parameter groups are specified in Table 3.

Table 3  
316L steel chemical composition after SEM analysis

Parameter group name	Laser power $L_P$ [W]	Exposure velocity $e_v$ [mm/s]	Hatching distance $h_d$ [mm]	Energy density $\rho_E$ [J/mm <sup>3</sup> ]
S_01	190	900	0.12	58.64
S_15	200	810	0.13	63.31
S_17	180	990	0.13	46.62
S_27	180	810	0.11	67.34
S_30	120	300	0.08	166.67

All five groups of parameters were used to produce samples for structural analysis, including microstructure investigation and residual stress measurement: sclerometric hardness testing, and tensile tests. The second part of the research used hot isostatic pressing on two selected groups of parameters – S\_01 and S\_17. After heat treatment, all of the original tests were carried out.

Some of the samples (S\_01; S\_17 and S\_30) [28] were tested during the previous research. In this manuscript, a part of the previous research has been put and extended by additional test results and two parameter groups (S\_15 and S\_27). That kind of approach was used to justify sample selection for HIP treatment and keep the topic continuation of research [26] to make it easier to understand why S\_01 and S\_17 samples were selected for second-stage modifications.

The last part of the research was an additional test of S\_01 and S\_17 samples. The influence of solution heat treatment

on the samples made using the S\_30 parameters group was checked as well.

Specimens from each series were manufactured during a single process to assure the same material properties of each specimen from each group. Specimen manufacturing processes were carried out in an argon atmosphere with the oxygen content lower than 0.2%.

All specimens were oriented horizontally to ensure the highest possible strength and elongation of the additively manufactured specimens. For the prepared research program, it was necessary to reach the highest possible elongation to record the influence of the low-ranged changes in the process parameters.

Porosity and microstructure investigations were made using an Olympus LEXT OLS4100 confocal microscope. Specimens dedicated for porosity and microstructure analysis were mounted in resin and prepared for observation by grinding and polishing. For each specimen, the porosity was analyzed in the central part of the metallographic section. All visible pores were marked in both analyzed planes. Porosity quantitative analysis was based on the captured microscopic images. It was carried out using a Mountains Map 6 Software. To reveal the microstructure, samples were etched using an “acetic glycergia” solution. The solution composition was: 6 ml HCl, 4 ml HNO<sub>3</sub>, 4 ml CH<sub>3</sub>COOH and 0.2 ml glycerol. To reach the proper effect, 40 s etching time was applied.

To determine the surface residual stresses, diffractometric measurement was made of the values of  $\sigma_1$  and  $\sigma_2$ , two main, perpendicularly oriented directions of the distribution of residual stresses,  $\sin^2\psi$ . The measurements were made using a Bruker D8 Discover X-ray diffractometer with the Euler wheel and the sample positioning system in three axes.

The samples for the research were prepared by separating part of the material from the end of the specimens for tensile testing by electrical discharge machining. This particular type of machining had been used to avoid measurement interference based on the available research conclusions [30]. Radiation and beam optics were specially prepared for the specimen measurements and were characterized by CoK $\alpha$  filtration series, polycapillary primary beam optics with  $\varnothing$ 1.0 mm pinhole collimator, parafocous secondary beam optics with a positionally sensitive semiconductor LYNXEYE detector with a 2.6° span in 2 $\theta$  angle, and parallel beam optics for a secondary beam with a Soller collimator with 0.23° equatorial divergence. The standard diffractometric measurements of residual stresses were used. For the qualitative phase analysis, CrystalImpact Match! 3 software was used with an ICDD PDF-4+ 2019 crystallographic database.

Sclerometric hardness testing was conducted using the Center for Tribology, Inc. (CETR) Universal Nano & Micro Tester. This device enables a comprehensive assessment of the mechanical and tribological properties of thin coatings and solid materials; depending on its configuration, it allows you to carry out various tests on a nano, micro, and macro scale. To determine the sclerometric hardness, three scratches were performed for each specimen; additionally, for each scratch, three width measurements were made which gave nine measurements for each specimen. The measurement error was calculated using the exact differential method.

Sclerometric hardness measurements were based on the analysis of the average width of a scratch made by an indenter with specified geometry. During material scratching, there is a constant normal load with additional constant indenter movement speed. This method is helpful to test the hardness of the material in nano, micro, and macro scales. This kind of hardness test enables the analysis of the additively material layered structure on the perpendicular surface to the building platform. The sclerometric measurements were compared to test results made

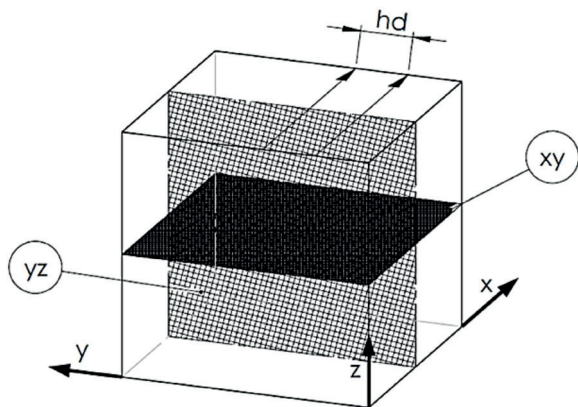


Fig. 3. Cubic specimen showing two main tested surfaces: xy – plane parallel to the building platform surface; yz – plane perpendicular to the building platform surface; hd – hatching distance between the exposure lines; Z – the direction of layers growth [25]

on X surfaces parallel to building platforms. The described surfaces are shown in Fig. 3.

Axial tensile strength tests of additively manufactured samples made of 316L steel were carried out according to ASTM E466–96 with the use of the hydraulic pulsator, Instron 8802. Measurements of elongation under axial stretching were obtained using an Instron 2630–112 extensometer with a measuring base of 25 mm. All samples subjected to axial tension had the same geometry.

To analyze the chemical composition, EDS (electron backscatter diffraction) module in SEM (scanning electron microscope) Jeol JSM-6610 (JEOL Ltd, Tokyo, Japan) has been used. Deformations of the material during tensile tests were recorded using the DIC method. The analyses were carried out using the Dantec Q – 400 Series system, while data processing was carried out in the ISTR4 4D software. Deformation observations were made from the front surface of the analyzed samples. Deformation results were compared with the registered strain values after tensile testing.

### 3. Microstructure analysis – results and discussion

Microstructure observations were performed on two different surfaces in reference to the machine-building platform – perpendicular and parallel. Additive manufactured parts could be characterized by six main porosity types:

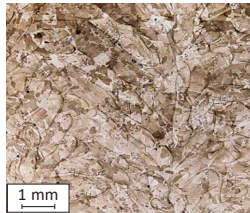
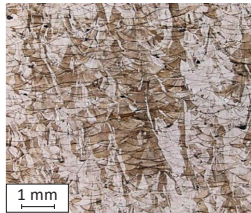
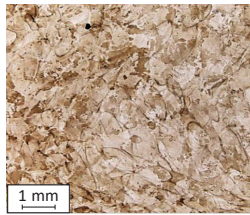
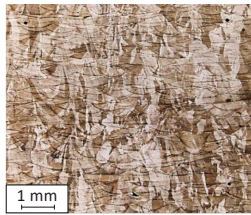
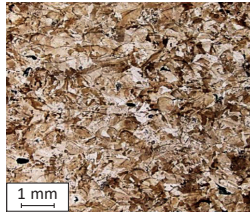
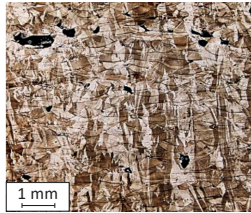
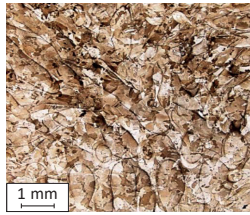
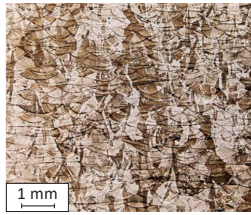
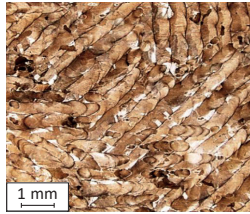
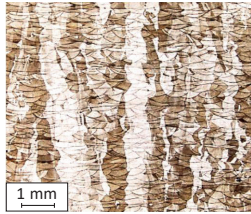
- 1) Gas porosity
- 2) Keyhole porosity
- 3) Lack of fusion porosity
- 4) Borderline porosity
- 5) Share of non-melted grains
- 6) Porosity caused by the balling effect.

The main reason for porosity generation is wrong process preparation or using non-optimized process parameters.

On some specimen surfaces, porosity could be seen as black, non-regular shapes.

The use of five different groups of parameters revealed that parameter modification mainly affects the porosity between the layers, visible in the figures of Table 4 on the perpendicular surfaces to the building platform.

Table 4  
Microstructure of specimens: two cross-sections

Specimen description	Surface parallel to the building platform	Surface perpendicular to the building platform
S_01		
S_15		
S_17		
S_27		
S_30		

As was described in [25] and shown in Table 4, the S\_17 specimen has visible porosity on a much higher level than other specimens.

The porosity is mainly caused by the gas porosity and the share of non-melted grains in the material volume. During the microstructure investigation, a homogeneous distribution of the spherical pores was observed (Fig. 4).

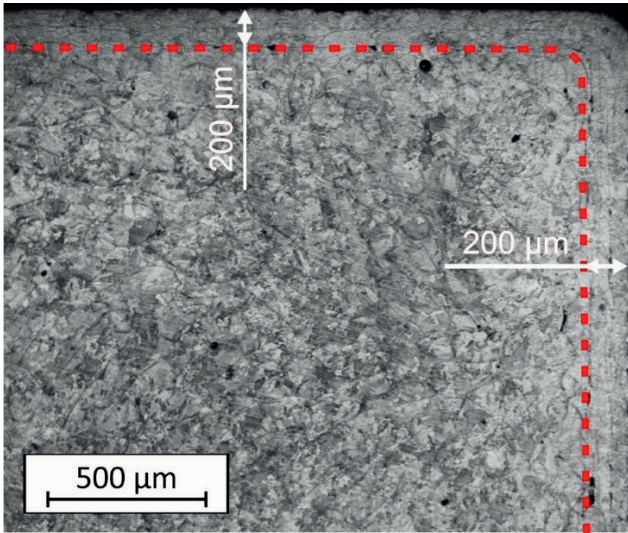


Fig. 4. Microstructure in the core and border outline areas

Comparing the microstructure of the S\_01 and S\_30 specimens, smaller grain size was observed in the S\_30 specimen. This phenomenon relates to the latter's three times higher

energy density, which caused more shrinkage due to the higher level of the temperature gradient after exposure.

The microstructure analysis allows registering the border outline shape on the parallel surface to the building platform. As can be seen in Fig. 4, there are no visible gaps between the core and border outline areas.

No imperfections were observed between borderline and core in any specimens. This was achieved by using different parameters for the outline shell than in the core of the exposure area. In accordance with own research, the default parameters of the machine producer for the 316L steel material were used.

#### 4. Parameter modification influence on residual stresses – results and discussion

Based on the monocrystalline elastic constants for austenitic steel ( $C_{11} = 204.0$  GPa,  $C_{12} = 133.0$  GPa,  $C_{44} = 126.0$  GPa), the elastic constants of the specimens were determined using the Reuss model [31]. The obtained values were, respectively,  $E_{311} = 144.5$  GPa,  $\nu_{311} = 0.35$  and  $E_{111} = 298.1$  GPa,  $\nu_{111} = 0.18$ . The residuals stress determined by measuring the Fe 111 reflection positions lies within the measurement uncertainty with the expansion coefficient  $k = 1$  or, for some specimens,  $k = 2$ , with the results obtained from Fe 311 reflex measurements.

Detailed test results were presented using a measuring series based on 311 reflection analysis, because these results, due to the angular position of the Fe 311 peak, are more resistant to systematic measurement errors. The residuals stress measurements with their orientation directions are shown on the chart (Fig. 5).

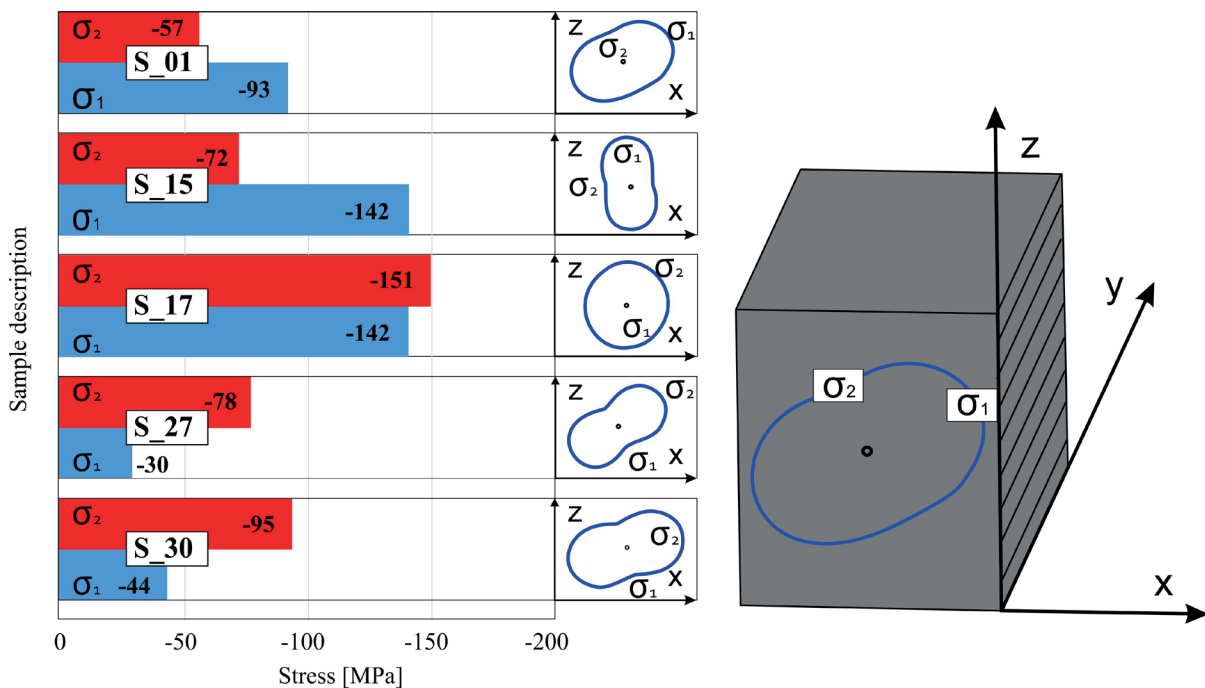


Fig. 5. Vertical and horizontal residual stresses ( $\sigma_1$  is parallel to x axis,  $\sigma_2$  is parallel to z axis)

Sample orientations in the diffractometer are shown in the circular diagrams of directional stresses in Fig. 4, indicating directions and values of main stresses. Stress orientation is presented according to the additive-manufacturing directions of the specimens: the vertical direction in the visualization corresponds to the direction parallel to the building platform, and the horizontal direction corresponds to the surface perpendicular to the building platform. All uncertainties are given with the coverage factor  $k = 1$ .

As can be seen in Fig. 4, all additively manufactured specimens indicate compressing stresses, which were caused by the high-temperature gradient during the manufacturing process.

Residual stresses in specimens manufactured using much higher energy density (S\_30) were much lower than expected. The main reason for this phenomenon may be connected with the use of cutouts from bigger specimens. One of the research goals was to discover the level of residual stresses after removing a part of the material. The biggest registered residual stress level was in the S\_17 specimen, where the greatest porosity was recorded. That level of residual stress could be connected with the porosity formation.

## 5. Measurements of sclerometric hardness – results and discussion

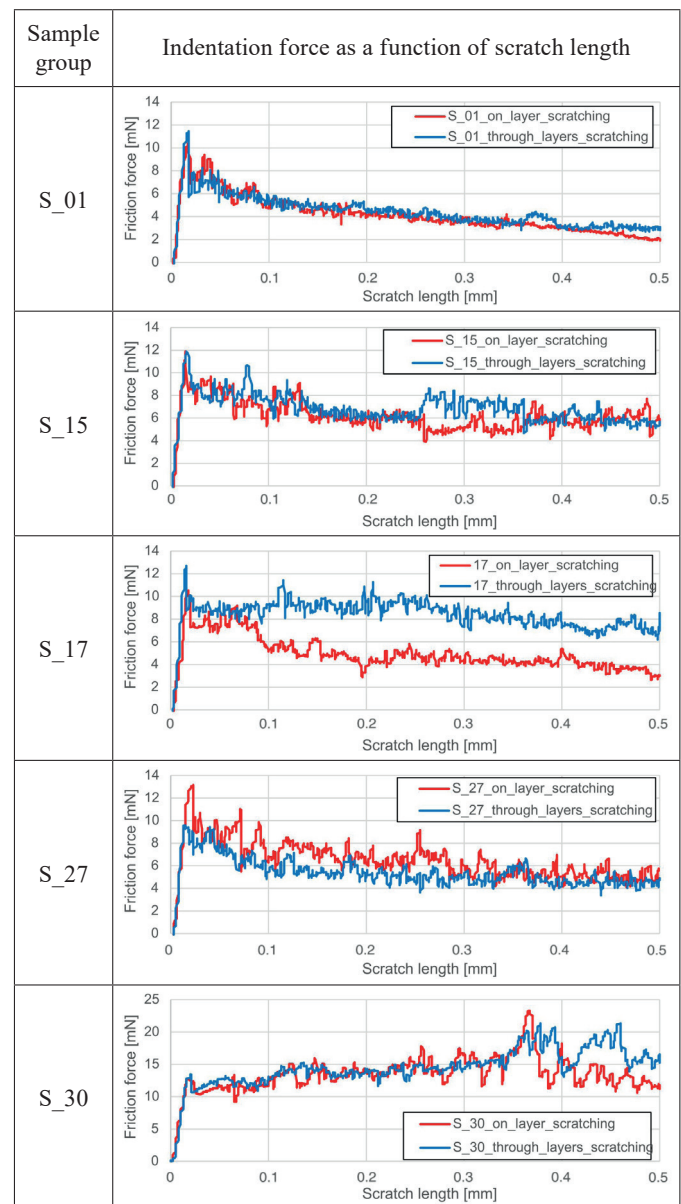
**5.1. Friction force measurement.** An additional measurement included in this research was friction force as a function of scratching length. Measurements were made on both surfaces – parallel and perpendicular to the machine-building platform. That analysis helped to identify any visible differences between the material structure on the surface parallel to the building platform versus the cross-section through the layers perpendicular to the building platform. The results for each specimen are shown in Table 5.

The charts shown in Table 5 were compared across all measurements. Differences between the force values for each layer are especially visible in S\_17 specimens. These issues are not a result of different material properties but with the surface curvature imperfections of some specimens.

During the measurement, the entire system was calibrated in accordance with standards to ensure proper force values during scratching. In almost all specimens, excluding S\_30, there are visibly higher force fluctuations in the surface perpendicular to the building platform than in the surface parallel to the building platform. In the S\_30 sample, this phenomenon is not visible. Based on these results, we conclude that in the standard range of energy density values the layered structure of the material is noticeable during cross-sectional scratching of the surface through the material layers. When using much higher energy density values during the process, the layered structure characteristic was not recorded. This may be the result of the material melting in the volume deeper than single-layer height due to the much higher energy delivered to the material.

**5.2. Sclerometric hardness measurement.** Based on the recorded scratching force and the scratch dimensions, it was pos-

Table 5  
Friction force as a function of scratch length



sible to calculate the sclerometric hardness using the equation parameters associated with the indenter (2):

$$HS_p = \frac{8F}{\pi \cdot w^2} \quad (2)$$

where:  $H_{Sp}$  – sclerometric hardness [Pa];

$F$  – normal force [N];

$w$  – average scratch width [m].

Measurements were made for both analyzed orientations (Fig. 6).

Lower sclerometric hardness values were found across the through layers (perpendicular to the building platform) rather than on the layers in specimens S\_17 and S\_27. Regarding sclerometric hardness, results for S\_01 and S\_15 specimens

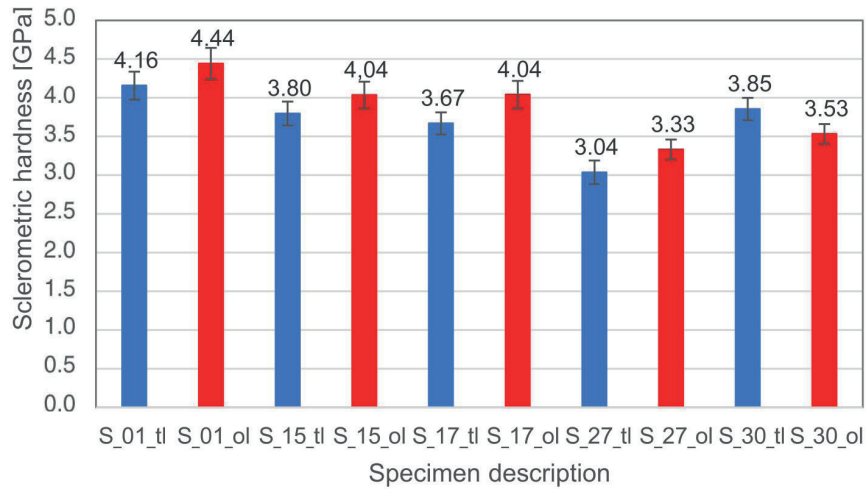


Fig. 6. Sclerometric hardness measured in both directions in relation to the machine-building platform – on layer (ol) and through layers (tl) with error bars determined using exact differential method

with measurement error considered, the registered values are nearly similar which could be connected with higher laser power used during manufacturing those specimens. The opposite phenomenon was found in the S\_30 group, where sclerometric hardness was significantly higher in the “on layer” surface, above the calculated measurement error.

### 6. Tensile strength and displacement measurements using DIC – results and discussion

To expand the analyses, conventionally made test parts of the same material were subjected to uniaxial, quasi static and cross-head controlled tensile testing.

Specimens were cut out of the cold-rolled sheet with a rolling direction consistent with the direction of exposure in additively manufactured samples. The results of tensile testing on the samples produced by the SLM technology with 316L steel are shown in Fig. 7, where  $R_{0.2}$  is proof strength,  $R_m$  is tensile strength and A is percentage elongation after fracture.

The highest tensile strength was reached using the S\_01 parameter group, whereas the lowest tensile strength value was recorded during S\_17 sample testing. The results indicate over 40% reduction in relative strain, 16% reduction in tensile strength and 20% decrease in yield strength for specimens manufactured using parameter group S\_17 compared to the S\_01 group, which is the recommended parameter set by the manufacturer of the SLM 125HL system. Using the S\_27 parameter

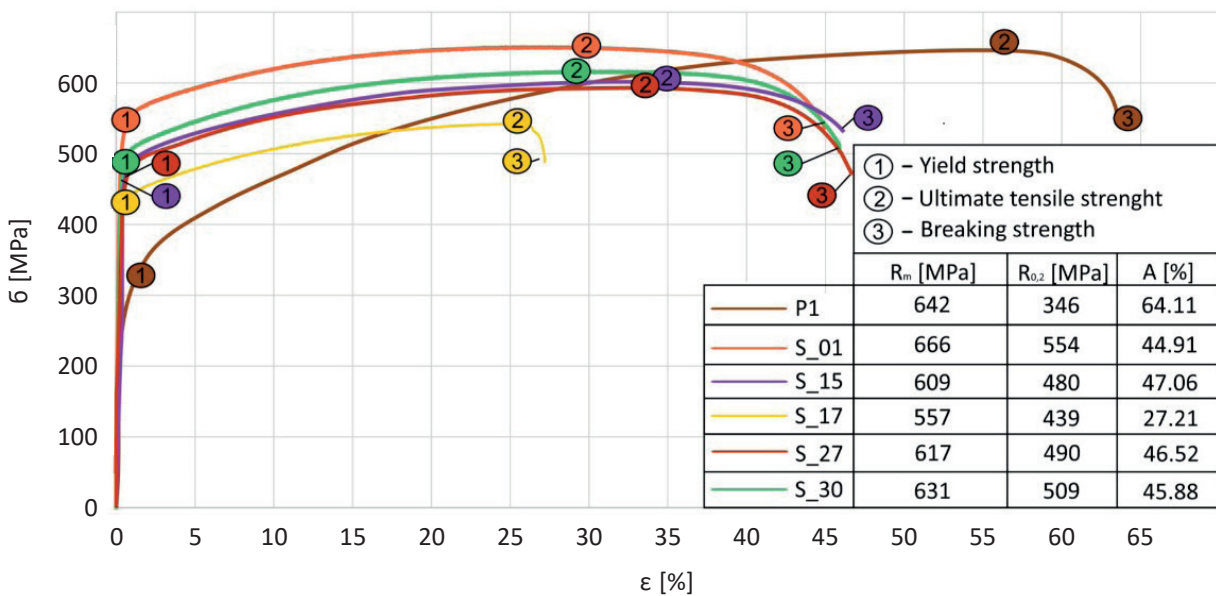


Fig. 7. Stress-strain curves for S\_01, S\_15, S\_17, S\_27 and S\_30 samples with the recorded waveform for a conventionally produced specimen (P1) with marked characteristic points recorded during digital image correlation

group facilitated reaching the largest relative strain among all tested samples.

The observed decrease in ultimate tensile strength ( $R_m$ ) value is affected by increases in the hatching distance and exposure velocity and is also related to reduce the laser power. These three parameters affect the energy density (Eq. (1)). All mentioned parameter modifications decrease the energy delivered into the volume of the material.

Tensile test results with marked places of occurrence of characteristic quantities (yield strength, ultimate tensile strength, and breaking strength) are presented in Fig. 5. The recorded deformation values for these characteristic values are shown in Fig. 8.

phenomenon relates to a high amount of porosity inside the S\_17 sample volume.

For samples P1, S\_01, S\_15, S\_27, and S\_30 (Fig. 8c), maximum deformations were observed near the crack initiations. Cumulation of the maximum deformations in one place and the uniform nature of their growth indicate that additively manufactured parts are stabilized throughout the load range. In the area with high deformation value (Fig. 8c), necking is visible, which proves the high plasticity of the manufactured material. There were no local or band heterogeneities of deformations, which in a wide range of load changes makes it impossible to predict the location of the crack initiation.

### 7. Heat treatment – hot isostatic pressing – results and discussion

Additively manufactured specimens using two sets of parameter groups, S\_01 and S\_17, were obtained using HIP. The specimens received HIP treatment in an argon atmosphere at 1150°C under pressures equal to 100 MPa for 3 h. The process was preceded by heating with a speed of 600°C per hour with the input pressure equal to 40 MPa. After the annealing process, the cooling rate was equal to 400°C per hour.

Specimen selection was based on the preliminary test results, in which the S\_01 specimen group was characterized by the best tensile properties and the S\_17 group had the worst. The primary purpose of HIP annealing was to check the ability of the process to improve the structure and mechanical properties from both selected parameter groups. After HIP treatment, all measurements and analyses shown in this article were conducted on annealed specimens with the addition of the porosity analysis, which were carried out in preliminary research [26]. The first analysis compared porosity before and after HIP annealing. Table 6 shows the results before and after HIP for specimens manufactured using parameter groups S\_01 and S\_17.

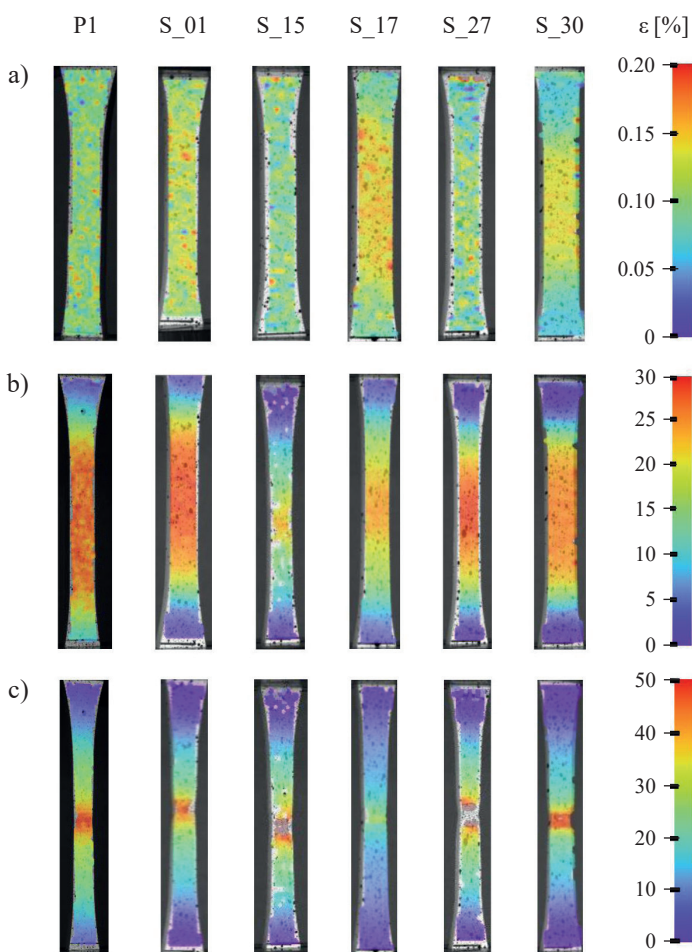


Fig. 8. Deformation distributions of three characteristics recorded during digital image correlation tests for each sample: a) yield strength, b) ultimate tensile strength and c) breaking strength

The results obtained during DIC (Fig. 8) indicate a homogeneous deformation distribution over the entire surface for all analyzed samples. A visible difference was observed in the deformation distributions of the S\_17 samples, where after exceeding the yield point (Fig. 8b) areas of almost equal material deformation were observed. The same samples did not show visible necking after reaching the breaking point. This

Table 6  
 Porosity in two main orientations:  
 xy – plane parallel to the building platform surface,  
 yz – plane perpendicular to the building platform surface

Specimen description	Porosity before HIP [%]	Porosity after HIP [%]
S_01 – xy	0.171	0.043
S_01 – yz	0.184	0.036
S_17 – xy	0.879	0.195
S_17 – yz	0.957	0.335

After the HIP process, significant porosity reduction was observed on both surfaces of the S\_17 specimen. The porosity reduction was equal to 78% in the xy plane and 65% in the yz plane. No significant change in porosity was observed in either orientation of the S\_01 specimens because of low



Table 7

Microstructure along two main orientations: xy – plane parallel to the building platform surface, yz – plane perpendicular to the building platform surface

Specimen description	Before HIP	After HIP	Specimen description	Before HIP	After HIP
S_01 – xy			S_17 – xy		
S_01 – yz			S_17 – yz		

porosity directly after the additive manufacturing process. The phenomenon of porosity reduction can be observed in Table 7, where the microstructures of S\_01 and S\_17 before and after heat treatment are shown. Additionally, HIP treatment reduced mostly porosity caused by a share of non-melted grains, small pores caused by gas porosity were not completely removed from the material volume.

The second analysis was on microstructural changes caused by HIP annealing. Similar to porosity analysis, the microstructure investigation was conducted on specimens from both selected groups, S\_01 and S\_17. The microstructures are shown in Table 7.

Porosity reduction is visible in the microstructure of both analyzed orientations in the S\_17 specimens. For both S\_01 and S\_17, the same microstructural changes are visible after HIP annealing. Microstructure is characterized by polygonal austenite grains that are typical for austenitic steels. Slow cooling after HIP annealing caused grain growth after the process in both directions. The grain distribution direction is strictly connected with the distribution of exposure lines in the xy plane and with the layer deposition direction for the yz plane.

The last type of structural analysis was residual stress measurement. Figure 9 provides a bar chart comparison of residual stresses before and after HIP annealing.

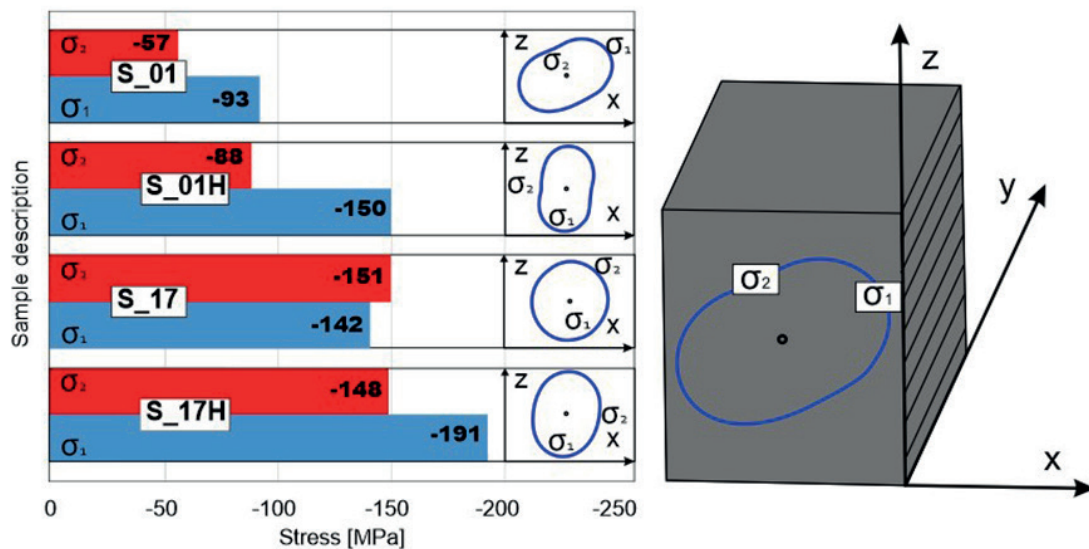
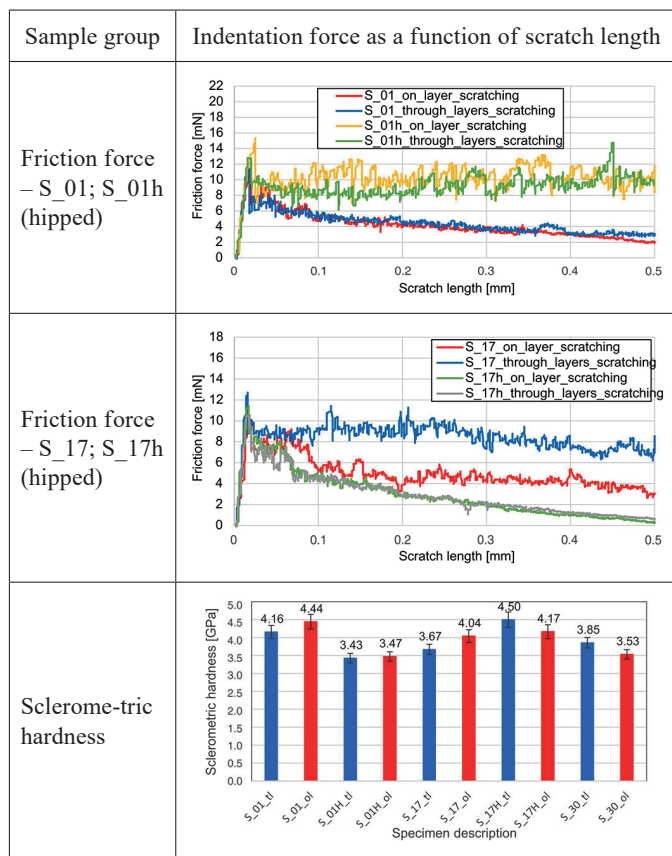


Fig. 9. Residual stress comparison after HIP process ( $\sigma_1$  is parallel to x axis,  $\sigma_2$  is parallel to z axis)

**Table 8**  
Friction force as a function of scratch length and sclerometric hardness after HIP annealing



After HIP annealing, significant growth (30–40%) of residual stress is visible in the perpendicular plane in both S\_01 and S\_17 specimens which were shown as S\_01H and S\_17H in

Fig. 9. This phenomenon could relate to the consolidation of the material near the borders and generation of layers of additional stress in that area. Residual stresses are strictly dependent on the part of geometry. In all cases the tested samples have compressive stresses, which is a result of the research design method using cutouts from the same part of each sample.

Sclerometric hardness measurements were conducted on the samples HIP influence on all these parameters are shown in Table 8.

Different measurements of sclerometric hardness show an opposite behavior of S\_01 and S\_17 specimens after HIP. Fluctuations in S\_01 force are much higher after HIP, whereas in S\_17, the fluctuations are almost at the same level before and after HIP. This phenomenon appeared also in sclerometric hardness measurements, where there is a significant decrease in the material hardness after HIP in S\_01 specimens and no consistent relationship between HIP and sclerometric hardness in S\_17 specimens. Additionally, in S\_01 specimens there is almost the same sclerometric hardness level which could relate to higher material isotropy after that kind of heat treatment. Also, in S\_17 specimens this phenomenon is visible, because of measurement errors overlapping in some extent.

The last group of analyses consisted of tensile tests with DIC measurements of specimen strain during tensile testing. Figure 10 depicts the characteristics of additively manufactured specimens after heat treatment. A significant strain increase was observed in both types of samples, S\_01H and S\_17H.

Samples receiving HIP treatment S\_01 had a 30% higher strain of the element in comparison to additionally manufactured elements without any heat treatment. More significant improvement was observed in S\_17, where strain increased by 50%. As can be seen in Fig. 11, both waveforms S\_01H and S\_17H significantly approached the waveform recorded for

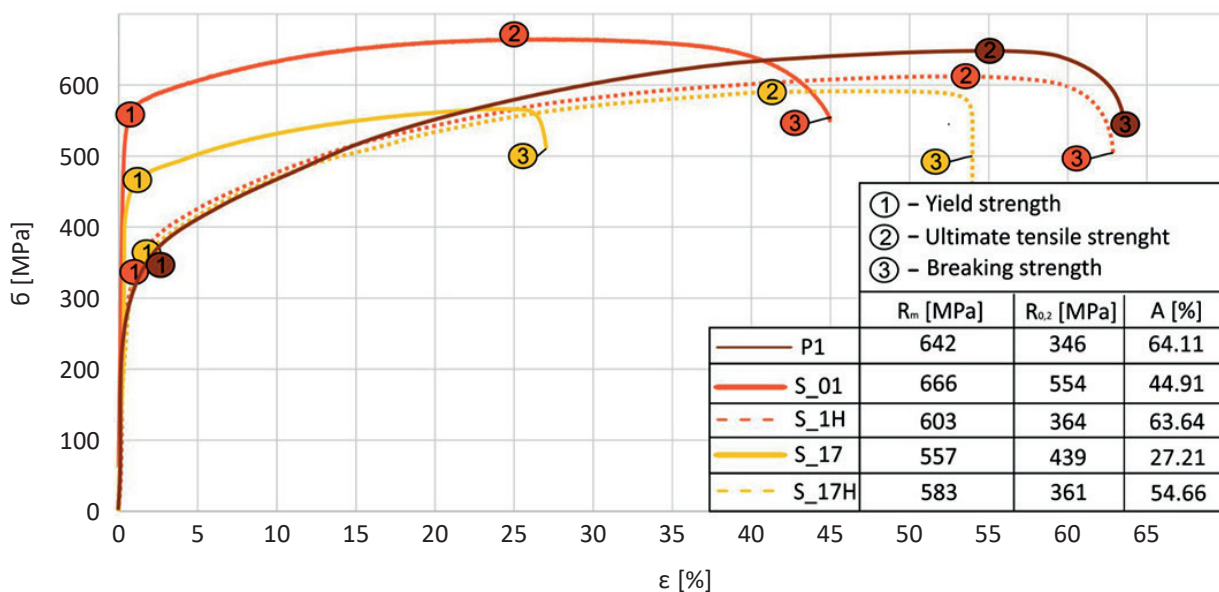


**Fig. 10.** Stress-strain curves for additively manufactured samples before (S\_01, S\_17) and after heat treatment (S\_01H, S\_17H) and for conventionally produced elements (P1)

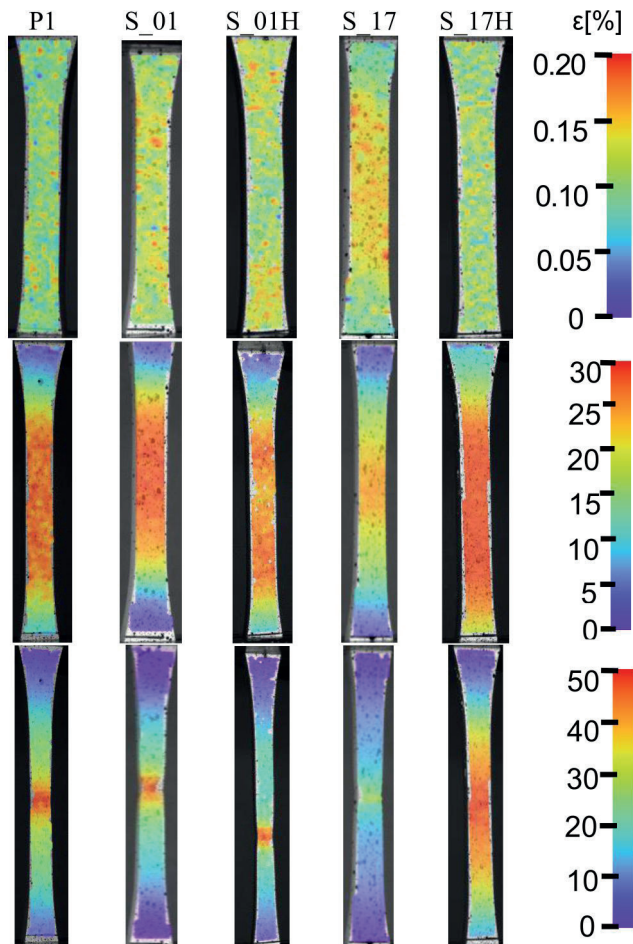


Fig. 11. Deformation distributions recorded during digital image correlation tests before and after heat treatment

conventionally produced material (which was tested in without additional heat treatment condition).

Deformation distribution in all samples up to the breaking point is characterized by very high uniformity.

In HIP treated specimens, the results of deformation measurements are similar to the conventionally produced samples (P1 in Fig. 11). In the case of the S\_01H and S\_17H specimens, no local or band heterogeneities of deformations were found, which in a wide range of load changes makes it impossible to predict the location of the crack initiation.

## 8. Conclusions

Understanding the phenomena of using different process parameters in SLM processing and heat treatment on the material microstructure and mechanical properties is very helpful during the design of special purpose constructions. Based on the results obtained in this study, the following conclusions could be drawn.

Energy density reduction of 20% caused almost a 50% decrease in elongation and a 10% decrease in tensile strength. Additionally, manufacturing using parameters with lower energy density had no visible sample necking during tensile testing.

The layered structure surfaces tested in a cross-section perpendicular to the building platform was observed. Using higher values of energy density during the SLM process and using HIP eliminates the layered structure effect and reduces the surface roughness with the growth of the material solidification.

Regarding obtained research results, HIP treatment is the most desirable in selective laser melted parts, characterized by increased porosity (as S\_17 samples in the attached research result in this manuscript). According to HIPped dense samples (S\_01), HIP treatment reduced layered structure and increased compressive residual stresses without any additional influence on the material structure.

Porosity generation based on the non-melted grains and lack of fusion caused a higher level of residual stresses in the material structure. Additional heat treatment using HIP caused residual stress growth in the horizontal direction (along the layer deposition direction) due to the recrystallization of the materials in the volume of pressed powder grains which were not melted in the SLM process.

Additional heat treatment using HIP did not cause greater necking in the samples during tensile testing of the S\_17 samples, which were characterized by higher porosity. DIC analysis revealed that increased levels of elongation relate to the wide range of the specimen deformation in the front surface areas.

**Funding.** The Programme is co-financed by the European Social Fund under the “Knowledge Education Development Operational Programme” in 2014–2020. The research was also partially supported by the university research grant No. 22–758.

## REFERENCES

- [1] A. du Plessis *et al.*, “Beautiful and Functional: A Review of Bio-mimetic Design in Additive Manufacturing”, *Addit. Manuf.* 27, 408–427 (2019).
- [2] L.E. Murr, “Frontiers of 3D Printing/Additive Manufacturing: from Human Organs to Aircraft Fabrication”, *J. Mater. Sci. Technol.* 32(10), 987–995 (2016).
- [3] P. Rokicki *et al.*, “Manufacturing of aircraft engine transmission gear with SLS (DMLS) method”, *Aircr. Eng. Aerosp. Technol.* 88(3), 397–403 (2016).
- [4] K.S. Prakash, T. Nancharaih, and V.V.S. Rao, “Additive Manufacturing Techniques in Manufacturing -An Overview”, *Mater. Today Proc.* 5(2), 3873–3882 (2018).
- [5] J. Robl, J. Sedlák, Z. Pokorný, P. Ńuksa, I. Barényi, and J. Majerík, “Analysis of advanced additive technology in direct metal laser sintering and precision casting method”, *Bull. Pol. Ac.: Tech.* 68(1), 109–118 (2020).
- [6] J. Kluczyński *et al.*, “The Examination of Restrained Joints Created in the Process of Multi-Material FFF Additive Manufacturing Technology”, *Materials (Basel)*. 13(4), 903 (2020).
- [7] J. Metelkova, Y. Kinds, K. Kempen, C. de Formanoir, A. Witvrouw, and B. Van Hooreweder, “On the influence of laser defocusing in Selective Laser Melting of 316L”, *Addit. Manuf.* 23, 161–169 (2018).
- [8] J. Kluczyński *et al.*, “Comparison of different heat treatment processes of selective laser melted 316L steel based on analysis of mechanical properties”, *Materials (Basel)*. 13(17), 3805 (2020).

- [9] J. Kluczyński *et al.*, “Crack growth behavior of additively manufactured 316L steel-influence of build orientation and heat treatment”, *Materials (Basel)*. 13(15), 3259 (2020).
- [10] A. Antolak-Dudka *et al.*, “Static and dynamic loading behavior of Ti6Al4V honeycomb structures manufactured by Laser Engineered Net Shaping (LENSTM) technology”, *Materials (Basel)*. 12(80), 1225 (2019).
- [11] M. Kuciewicz, P. Baranowski, J. Małachowski, A. Popławski, and P. Płatek, “Modelling, and characterization of 3D printed cellular structures”, *Mater. Des.* 142, 177–189 (2018).
- [12] J. Maszybrocka, A. Stwora, B. Gapiński, G. Skrabalak, and M. Karolus, “Morphology and surface topography of Ti6Al4V lattice structure fabricated by selective laser sintering”, *Bull. Pol. Ac.: Tech.* 65(1), 85–92 (2017).
- [13] M. Kuciewicz, P. Baranowski, M. Stankiewicz, M. Konarzewski, P. Płatek, and J. Małachowski, “Modelling and testing of 3D printed cellular structures under quasi-static and dynamic conditions”, *Thin-Walled Struct.* 145, 106385 (2019).
- [14] N. Kalentics, E. Boillat, P. Peyre, S. Ćirić-Kostić, N. Bogojević, and R. E. Logé, “Tailoring residual stress profile of Selective Laser Melted parts by Laser Shock Peening”, *Addit. Manuf.* 16, 90–97 (2017).
- [15] W. Macek, D. Rozumek, and G.M. Królczyk, “Surface topography analysis based on fatigue fractures obtained with bending of the 2017A-T4 alloy”, *Meas. J. Int. Meas. Confed.* 152, 107347 (2020).
- [16] W.M. Tucho, V.H. Lysne, H. Austbø, A. Sjolyst-Kverneland, and V. Hansen, “Investigation of effects of process parameters on microstructure and hardness of SLM manufactured SS316L”, *J. Alloys Compd.* 740, 910–925 (2018).
- [17] D. Leordean, C. Dudescu, T. Marcu, P. Berce, and N. Balc, “Customized implants with specific properties, made by selective laser melting”, *Rapid Prototyp. J.* 21(1), 98–104 (2015).
- [18] A. Röttger, K. Geenen, M. Windmann, F. Binner, and W. Theisen, “Comparison of microstructure and mechanical properties of 316L austenitic steel processed by selective laser melting with hot-isostatic pressed and cast material”, *Mater. Sci. Eng. A* 678, 365–376 (2016).
- [19] A. Riemer, H.A. Richard, J. P. Brüggemann, and J.N. Wesendahl, “Fatigue crack growth in additive manufactured products”, *Frat. ed Integrita Strutt.* 9(34), 437–446 (2015).
- [20] J. Kunz, A. Kaletsch, and C. Broeckmann, “Influence of HIP post-treatment on the fatigue strength of 316L-steel produced by selective laser melting (SLM)”, *World PM 2016 Congr. Exhib.*, 2016.
- [21] B. AlMangour, D. Grzesiak, and J.M. Yang, “Scanning strategies for texture and anisotropy tailoring during selective laser melting of TiC/316L stainless steel nanocomposites”, *J. Alloys Compd.* 728, 424–435 (2017).
- [22] K. Ścigała, R. Bedziński, J. Filipiak, E. Chlebus, and B. Dyla, “Application of generative technologies in the design of reduced stiffness stems of hip joint endoprosthesis”, *Arch. Civ. Mech. Eng.* 11(3), 753–767 (2011).
- [23] J.J. Lewandowski and M. Seifi, “Metal Additive Manufacturing: A Review of Mechanical Properties”, *Annu. Rev. Mater. Res.* 46(1), 151–186 (2016).
- [24] K. Geenen, A. Röttger, and W. Theisen, “Corrosion behavior of 316L austenitic steel processed by selective laser melting, hot-isostatic pressing, and casting”, *Mater. Corros.* 68(7), 764–775 (2017).
- [25] L. Śniezek, K. Grzelak, J. Torzewski, and J. Kluczyński, “Study of the mechanical properties components made by SLM additive technology”, in *11th International Conference on Intelligent Technologies in Logistics and Mechatronics Systems, ITELMS 2016*, 2016, pp. 145–153.
- [26] J. Kluczyński, L. Śniezek, K. Grzelak, and J. Mierzyński, “The influence of exposure energy density on porosity and microhardness of the SLM additive manufactured elements”, *Materials (Basel)*. 11(11), 2304 (2018).
- [27] J. Kluczyński, L. Śniezek, K. Grzelak, and J. Torzewski, “The influence of layer re-melting on tensile and fatigue strength of selective laser melted 316L steel”, in *12th International Conference on Intelligent Technologies in Logistics and Mechatronics Systems, ITELMS 2018*, 2018, pp. 115–123.
- [28] J. Kluczyński *et al.*, “Influence of Selective Laser Melting Technological Parameters on the Mechanical Properties of Additively Manufactured Elements Using 316L Austenitic Steel”, *Materials (Basel)*. 13(6), 1449 (2020).
- [29] D. Wang, Y. Liu, Y. Yang, and D. Xiao, “Theoretical and experimental study on surface roughness of 316L stainless steel metal parts obtained through selective laser melting”, *Rapid Prototyp. J.* 22(4), 706–716 (2016).
- [30] P. Mercelis and J. P. Kruth, “Residual stresses in selective laser sintering and selective laser melting”, *Rapid Prototyp. J.* 12(5), 254–265 (2006).
- [31] B. Kania, P. Indyka, L. Tarkowski, and E. Beltowska-Lehman, “X-ray diffraction grazing-incidence methods applied for gradient-free residual stress profile measurements in electrodeposited Ni coatings”, *J. Appl. Crystallogr.* 48(1), 71–78 (2015).